https://doi.org/10.5194/egusphere-2026-4946
Preprint. Discussion started: 23 September 2026

Remote HVGD Implying the Seismogenic Positions of 2025 Mandalay Earthquake Sequence

Yu Feng[1,2], Wenfei Mao[1,2*], Jia Li[1,2], Yifan Ding[1,2], Yuan Qi[3], Guokun Chen[4,5], Busheng Xie[6], Licheng Sun[1,2], Hong Tang[7], Lixin Wu[1,2*]

[1] School of Geoscience and Info-Physics, Central South University, Changsha, 410083, China.
[2] Laboratory of Geo-Hazards Perception, Cognition and Predication, Central South University, Changsha, 410083, China.
[3] Department of Geography, Faculty of Social Sciences, The University of Hong Kong, Hong Kong SAR, China.
[4] Faculty of Land and Resources Engineering, Kunming University of Science and Technology, Kunming 650093, China.
[5] Yunnan Key Laboratory of Quantitative Remote Sensing, Kunming University of Science and Technology, Kunming 650093, China.
[6] Guangdong Provincial Disaster Prevention and Mitigation Center, Guangzhou 510630, China.
[7] Faculty of Geographical Science, Beijing Normal University, Beijing 100875, China.

Corresponding author: Wenfei Mao (maowf2014@126.com); Lixin Wu (wulx66@csu.edu.cn)

Abstract. Pressure-stimulated rock currents (PSRCs), widely documented in laboratory rock-loading experiments, have been proposed as a mechanism for pre-seismic geomagnetic disturbances. However, the relationship between horizontal vectors of geomagnetic disturbance (HVGD) and seismogenic fault processes remains unclear, particularly during large earthquakes with complex aftershock sequences. Using geomagnetic data from a station in southwestern China, we develop a spatial intersection method to investigate this relationship along the Sagaing Fault during the 2025 Mw 7.7 Mandalay earthquake sequence. The method identifies intersections between the mapped fault trace and horizontal lines normal to HVGD vectors, thereby constraining potential seismogenic locations. The intersection points migrate systematically along the Sagaing Fault and correspond to the rupture corridor and major earthquakes in the sequence. Notably, their distribution region coincides with the independently identified supershear rupture segment. The inferred locations are supported by positive anomalies in satellite-observed microwave brightness temperature. We attribute these observations to PSRC generation associated with stress activation in peroxy-defect-bearing lithologies along the fault. Under increasing tectonic stress at depth, stress-sensitive positive holes may be generated near frictional regions and propagate upward, producing electric currents detectable as geomagnetic disturbances at remote stations. The retrieved PSRCs, ranging from 7.3 to 91.9 MA, are broadly consistent with estimates scaled from laboratory specimens to seismogenic rock volumes. These results suggest that remotely observed HVGD can constrain evolving seismogenic processes along known active faults. The proposed HVGD–fault intersection approach provides a simple ground-based remote sensing method for tracking potential seismogenic positions and their migration during large earthquake sequences.

https://doi.org/10.5194/egusphere-2026-4946
Preprint. Discussion started: 23 September 2026

1 Introduction

Earthquake is one of the most destructive natural disasters worldwide. According to the United States Geological Survey (USGS), more than 300 earthquakes with magnitudes ≥7.0 have occurred globally since the 21st century. Recent large evnets, such as the 2008 Mw 8.0 Wenchuan earthquake in China, which casued 69,227 fatalities, 17,923 missing persons and economic losses exceeding 800 billion RMB (Zhao et al., 2009), and the 2023 Mw 7.8 Nurdagi earthquake in Turkey, which resulted in more than 50,000 fatalities and economic losses exceeding 100 billion dollars (Chen et al., 2026), highlight the persistent threat posed by large tectonic earthquakes. Improving the monitoring of possible pre-seismic geophysical anomalies and better constraining the spatial evolution of seismogenic processes are important but remain highly challenging. Geomagnetic disturbances associated with earthquakes have been reported in a wide range of observational studies and and have been intrepreted as possible electromagnetic responses to the key phases of seismogenesis such as micro-fracture propagation and stress locking (Guan et al., 2025; Mao et al., 2025; Volvach et al., 2025). Previous investigations of earthquake-related geomagnetic anomalies have mainly focused on temporal variations in the three geomagnetic components, using time-domain (Chernogor, 2019; Yusof et al., 2022; Zulhamidia et al., 2023) and frequency-domain (Takla et al., 2012; Hattori et al., 2013; Syed et al., 2021; Hamidi et al., 2024) approaches. These studies have revealed temporal correlations between geomagnetic disturbances and earthquake occurrence in some cases. However, the spatial relationship between observed geomagnetic anomalies and the active seismogenic region remains insufficiently understood. In particular, whether the horizontal vector of geomagnetic disturbance (HVGD) contains directional information related to the location or migration of seismogenic processes along an active fault has not been systematically examined.

A possible physical mechanism for earthquake-related geomagnetic disturbances is the generation of pressure-stimulated rock currents (PSRCs). Laboratory experiments have shown that electric currents can be generated during the compression and fracturing of rocks. Freund et al. (2006) observed a significant surge of rock current during the instantaneous compression of igneous rocks, showing a positive correlation with rock stress variation. Mao et al. (2022) detected a stable step-like current followed by oscillatory currents of several hundred nanoamperes prior to the failure of diorite specimens, intensifying the pressure-stimulated rock current (PSRC) phenomenon at experimental scale. Sun et al. (2025) further confirmed the presence of PSRC in multiple rock loading experiments, and analyzed to its characteristics under different fracturing modes. These experimental observations provide laboratory-scale evidence that stress-activated electric currents may be generated in stressed rock volumes and may propagate away from the source region. The PSRC mechanism has commonly been interpreted in terms of stress activation of positive holes associated with peroxy defects in minerals. When rocks containing peroxy bonds are subjected to increasing tectonic stress, the breaking of peroxy bonds may activate mobile positive hole charge carriers. These charge carriers can propagate through the surrounding rock, potentially forming electric currents capable of producing measurable electromagnetic or geomagnetic disturbances (Freund et al., 2006; Freund, 2011; Mao et al., 2022; Sun et al., 2025; Sun et al., 2026). Because peroxy defects are considered widespread in crustal minerals, this mechanism provides a possible link between stress changes in seismogenic zones and electromagnetic anomalies observed at or above the Earth's surface.

Historical and recent observations also suggest that some earthquake-related electromagnetic phenomena may have directional or spatial significance. Prior to the 1858 Setubal earthquake, anomalous compass behavior was widely observed. As reported by The New York Times (1858) on November 11, 1858, navigational compasses exhibited significant and abnormal deviations. Similarly, abrupt deflection and abnormal shaking of magnet needle was noticed by students and geography teacher in a middle school classroom of Beichuan High School in China, located 120 Km away from the epicenter, about 13 minutes before the May 12, 2008, M7.9 Wenchuan earthquake (Liang et al., 2017). Enomoto et al. (2020) reported a geomagnetic declination approximately 40 minutes before the March 11, 2011, M9.0 Tohoku-Oki earthquake in Japan, and attributed it to the seismic-induced quasi-static current of 20–30 kA in the source region. Xie et al. (2023) identified the horizontal vectors of geomagnetic disturbance being spatio-temporally correlated with the occurred earthquake lights with the March 16, 2022, M7.3 Fukushima, Japan, earthquake, and attributed it to the upward-propagation of seismic rock current, which was estimated as 35 kA about. Through multi-sphere coupling analysis of pre-seismic anomalies manifested in Japan (2021–2023), Xie et al. (2025) further confirmed the activation of P-holes as well as the subsequent upward propagation of PSRC.

Despite these observations, several key questions remain unresolved. First, the directional relationship between observed geomagnetic anomaly and developing seismogenic zone. Second, the spatio-temporal relationship between geomagnetic anomaly and earthquake sequence including mainshock and aftershocks. Third, the quantitative characteristics of PSRC before the mainshock in comparison with its co-seismic and post-seismic.

On 28 March 2025 at 06:20 UTC, a major Mw 7.7 earthquake struck northern Myanmar near Mandaly. The epicenter was located near Mandalay city at 22.00°N, 95.92°E, with a focal depth of 30 km. The earthquake occurred along the Sagaing Fault, one of the most prominent active strike-slip fault systems in Southeast Asia. By 1 April 2025, 36 aftershocks with magnitude ranging from Mw 4.1 to 6.7 had been recorded, as shown in Fig. 1a and 1b. The event caused devastating impacts, resulting in 4355 fatalities, 7830 injured and 210 people were reported missing (Xu et al., 2025). Heki et al. (2026) utilized GNSS receivers to observe ionospheric electrons and identified pre-seismic anomalies in the Total Electron Content (TEC) before the Mandalay earthquake, suggesting that these variations were possiblely driven by PSRC induced by P-holes at the fault (Mao et al., 2022). These ionospheric anomalies indicate that substantial rock currents may have been present at the seismogenic fault during and before the occurrence of the Mandalay earthquake. Concurrently with these phenomena. During this earthquake sequence, remarkable geomagnetic disturbances were also recorded at the remote YNCH geomagnetic station in Chenghai, Yunnan Province, southwestern China. The YNCH station, located at 26.55°N, 100.71°E, is approximately 700 km northeast of the mainshock epicenter and was installed by the Geohazard PCP Laboratory of Central South University in 2023.

https://doi.org/10.5194/egusphere-2026-4946
Preprint. Discussion started: 23 September 2026

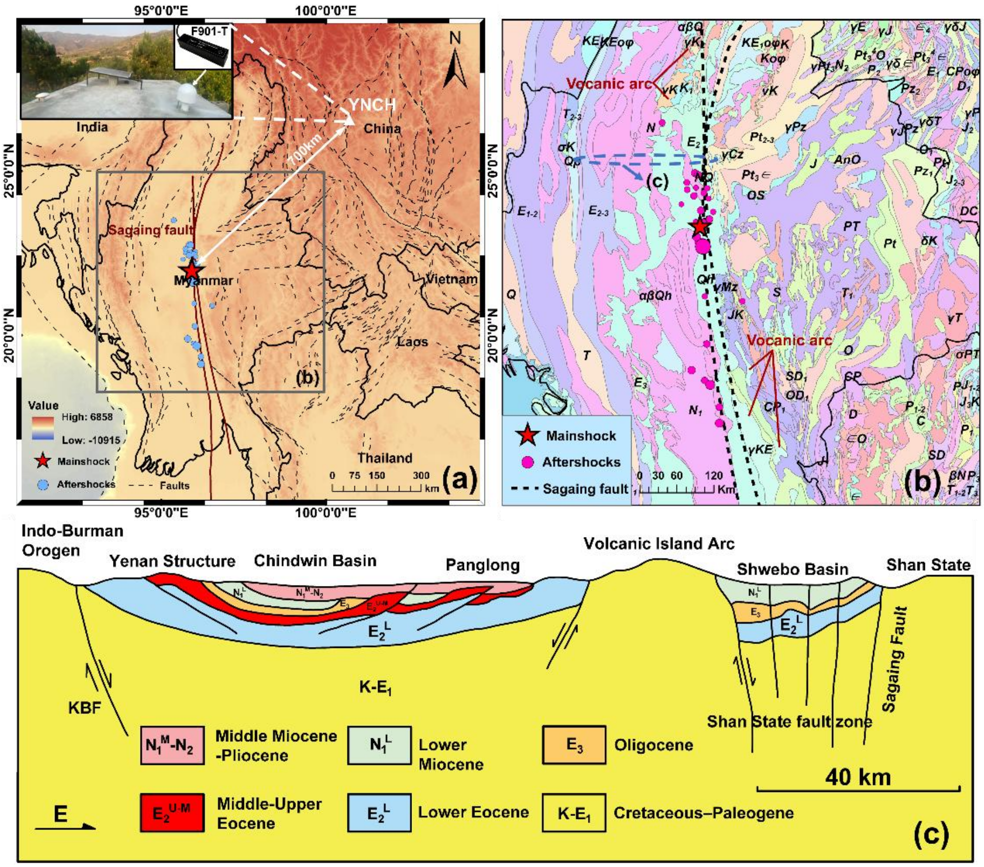

Figure 1: Map of the study area showing key sites and lithology distribution. (a) Geographical location map of the Mandalay earthquake sequence and geomagnetic stations. Earthquake data were obtained from the United States Geological Survey (USGS). The global active faults data were derived from Seismic Active Fault Survey Data Center. The digital elevation model was acquired from The General Bathymetric Chart of the Oceans（GEBCO Compilation Group. (2023)). **(b)** Stratigraphic lithology map. The rectangular area delineated in Fig. (a). Stratigraphic lithology data are modified from the 1:5M International Geological Map of Asia (Ren et al., 2013). The position of the volcanic island arc is based on Zhang et al. (2020). **(c)** Detailed lithology map of the subsurface. The region delineated in (b). The lithology map of the subsurface is modified Xie et al. (2010).

In this study, a forward spatial intersection method was developed referring to seismogenic fault and the normal line of HVGD, and applied to investigate the Mandalay earthquake with geomagnetic data recorded by YNCH. The spatio-temporal characteristics of the intersection points, with reference to the epicenters of the Mandalay earthquake sequence were carefully examined. Biot-Savart law was used to retrieve the PSRC generated by the seismic activity, and the area of positive anomaly of satellite microwave brightness temperature was used together to derive the PSRC intensity.

https://doi.org/10.5194/egusphere-2026-4946
Preprint. Discussion started: 23 September 2026

2 Data and Methods

2.1 Study area and geomagnetic station

The Mandalay earthquake sequence occurred in the central basin of northern Myanmar. From a regional tectonic perspective, the basin is located along the convergent boundary between the Indian and Eurasian Plates, and is characterized by intense seismic activities. The causative fault is identified as the Sagaing fault, which is a major tectonic structure resulting from the intrusion of the Indian Plate into the Eurasian Plate. It acts as a dextral strike-slip fault between the Myanmar Block and the Shan-Thai Block (Vigny et al., 2003). Extending for more than 1,400 km from the Andaman Sea to the eastern Himalayan syntaxis, the Sagaing fault is the most significant active fault in Myanmar. The southern segment of the fault exhibits a slip rate of approximately 18–23 mm/yr, while the northern segment moves at 10–15 mm/yr, reflecting notable along-strike variation in slip rates (Maurin et al., 2010). The activity of Sagaing fault is primarily governed by the combined effects of northeast-directed subduction and compressional forces from the Indian Plate against the Eurasian Plate (Tapponnier et al., 1982; Socquet et al., 2006). The fault surface is overlain by Quaternary marsh deposits, while the underlying bedrock is mainly composed of K-E1 (Cretaceous-Paleocene) igneous rocks such as diorite and andesite (Fig. 1b and 1c). The geomagnetic observation instrument of YNCH station is a F901-T triaxial fluxgate digital sensor, it made by Germany is capable of measuring three-dimensional geomagnetic fields with a measurement accuracy of the absolute horizontal magnetic field is 0.2% (about X: ± 29nT, Y: ± 8.8nT), operating on the principle of fluxgate technology. Additional details regarding the YNCH station are provided in Supplementary Material-Text S1.

2.2 Geomagnetic anomaly identification

Geomagnetic observations were recorded at a sampling rate of 1 Hz. Data spanning from January 2025 to April 2025 were selected for follow analysis. Due to instrumental errors and power supply fluctuations, the acquired data contained some anomalous and missing values (The raw geomagnetic data recorded at the YNCH station from January to April 2025 are shown in Supplementary Material-Fig. S2). Anomalous values were removed, and gaps were filled via spline interpolation to obtain a preprocessed dataset. Due to the substantial data volume, a moving average smoothing method was applied to resample the dataset to a 1-minute interval for analysis. Detailed preprocessing procedures are provided in Supplementary Material-Text S2.

In general, intense solar activity and geomagnetic storms have significant influences on the horizontal geomagnetic components (see Supplementary Material-Fig. S3 and Fig. S4). Under the condition of the Kp ≤ 4 (Kp index, is used to characterize the magnitude of geomagnetic storms (Xie et al., 2026)), such influence is relatively limited and can be considered negligible in this study. Thus, after excluding the influences of geomagnetic storms and solar activity disturbances, the daily geomagnetic curves should be exhibited high similarity in a month. Pearson correlation analysis is applied to assess the high similarity of the geomagnetic curves thereby eliminate geomagnetic curves affected by environmental magnetic disturbances. According to the evaluation criteria of Pearson correlation (Gao et al., 2007), cross-

https://doi.org/10.5194/egusphere-2026-4946
Preprint. Discussion started: 23 September 2026

correlation analysis is performed on all geomagnetic curves within a month that satisfy the condition of Kp ≤ 4. Curves with an average cross-correlation greater than 0.6 are retained as those less influenced by environmental magnetic disturbances. After preprocess by removing outliers and spline interpolating on recorded data, the daily geomagnetic data recorded by the YNCH station from Jan.1, 2025, to April 30, 2025, which satisfy Kp ≤ 4 and cross-correlation > 0.6, were selected for following analysis. After excluding the periods affected by the significant solar activity or environmental, geomagnetic components were obtained, which generally show diurnal variations throughout a month within a limited range. Therefore, the mean curve of each geomagnetic component within a month was adopted to represent the monthly geomagnetic background, and the correpoding standard deviation was employed to quantify the amplitude of baseline fluctuations.

The σ_1 and σ_2, calculated from January and February in 2025, were selected as reference for the background baseline fluctuation amplitude. From March 1st to 22th in 2025, σ3 was calculated as the reference for the background baseline fluctuation amplitude in March before the appearance of obvious geomagnetic anomalies in the long-term series geomagnetic curves, which started from March 23rd. According to the principles of probability statistics, over 99% of baseline fluctuation variations should fall within twice the standard deviation. Thus, the baseline fluctuation interval σ was defined as Eq. (1):

$$\sigma = 2\sqrt{\frac{\sigma_1^{\ 2} + \sigma_2^{\ 2} + \sigma_3^{\ 2}}{3}} \tag{1}$$

When a geomagnetic curve exhibits variations that clearly exceed the baseline fluctuation interval, it is considered as a geomagnetic anomaly.

2.3 Forward spatial intersection

Xie et al. (2023) proposed that pre-seismic horizontal geomagnetic disturbance anomalies are attributed to PSRC generated at the seismogenic zone or epicenter and propagated to ground surface. Based on the Biot–Savart law and the right-hand rule, they further developed a forward intersection localization method using pre-seismic HVGD at multiple stations, which successfully delineated the PSRC manifestation region (Xie et al., 2023; Xie et al., 2026). However, the Xie-method requires geomagnetic observations from at least two usable geomagnetic stations, and its positioning accuracy is highly sensitive to the angles between the normal line of HVGD derived from different stations.

To overcome these limitations, a simple forward spatial intersection method (illustrated in Fig. 2) was particularly developed for cases in which only one usable geomagnetic station is available but the geometry (position and strike) of the seismogenic active fault is well known. An iterative solver was designed to calculate the intersection point between the fault segment and the normal ray defined by HVGD, thereby pinpointing the manifestation position of PSRC at the active fault and enabling the positioning of seismogenic segment along the fault. In this case, the geometry of Sagaing fault is (dimensions: over 1,400 km in length; orientation: ~ 0–5° strike, ~ 60–90° dip), and the uncertainty of seismogenic positioning is relatively small (1.156′ deflection, [0.243km N, 0.928km S] about), which is primarily governed by the accuracy of geomagnetic

https://doi.org/10.5194/egusphere-2026-4946
Preprint. Discussion started: 23 September 2026

components observation (as in Fig. 2b). Detailed calculation procedures of the forward spatial intersection method see Supplementary Material-Text S3.

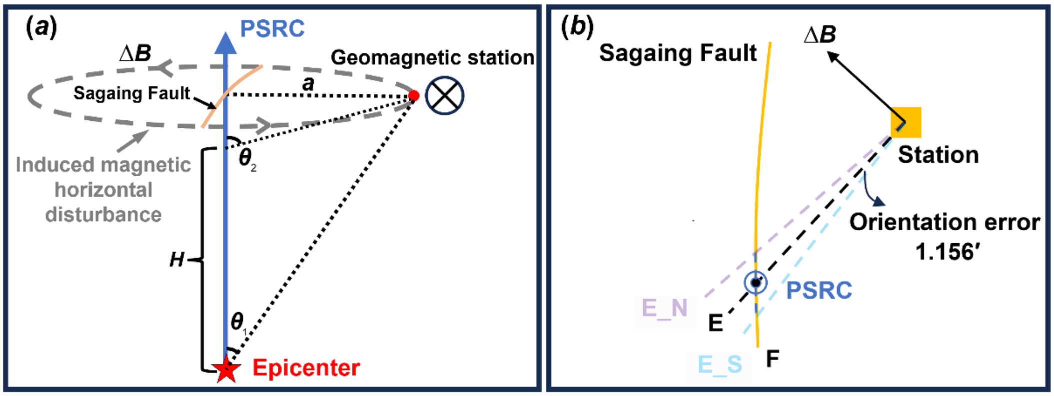

Figure 2: Principle of and error analysis to the simple forward spatial intersection. (a) Principles of seismicity-produced horizontal geomagnetic disturbance. At the laboratory scale, PSRC signals were observed immediately prior to failure in both centimeter-scale diorite samples (Mao et al., 2022) and larger diorite samples with better homogeneity (Sun et al., 2025) during loading experiments. At the seismic scale, the PSRC is characterized by a substantial magnitude and generates an induced magnetic field, thereby perturbing distant geomagnetic stations. (b) Single-station spatial intersection with seismic fault. The manifestation of seismogenic PSRC can be determined using remote sensed horizontal magnetic disturbance vector and known seismic fault based on the Biot-Savart law. The uncertainty of seismogenic positioning is narrow in this case study (1.156′ deflection, [0.243km N, 0.928km S] about).

3 Results

3.1 Geomagnetic anomaly before the mainshock

The daily geomagnetic data recorded at the YNCH station from January 1 to April 30, 2025, satisfying the criteri of $Kp \leq 4$ and cross-correlation > 0.6, are shown in Fig. 3. Both the X and Y components exhibited significant anomalous deviations exceeding the baseline fluctuation range from March 23 to March 31, with the anomaly in the Y component being particularly pronounced (see Fig. 3d). The Z component also displayed some variations beyond the baseline fluctuation range; however, these variations were not prominent and are therefore considered to fall within the range of normal fluctuations.

The anomalous variations observed in the horizontal components indicate significant changes in magnetic declination. As shown in Fig. 3b, 3c and 3d, the magnetic declination exhibited a clear anomalous westward deflection, with a maximum value of approximately 0.5224°，significantly exceeding the deflection caused by the uncertainty in seismogenic-source positioning. After excluding other possible sources of geomagnetic anomalies, such as environmental influence (The field investigations confirming no other environmental magnetic disturbances), these anomalies were considered as potential indicators associated with the Mandalay earthquake sequence.

https://doi.org/10.5194/egusphere-2026-4946
Preprint. Discussion started: 23 September 2026

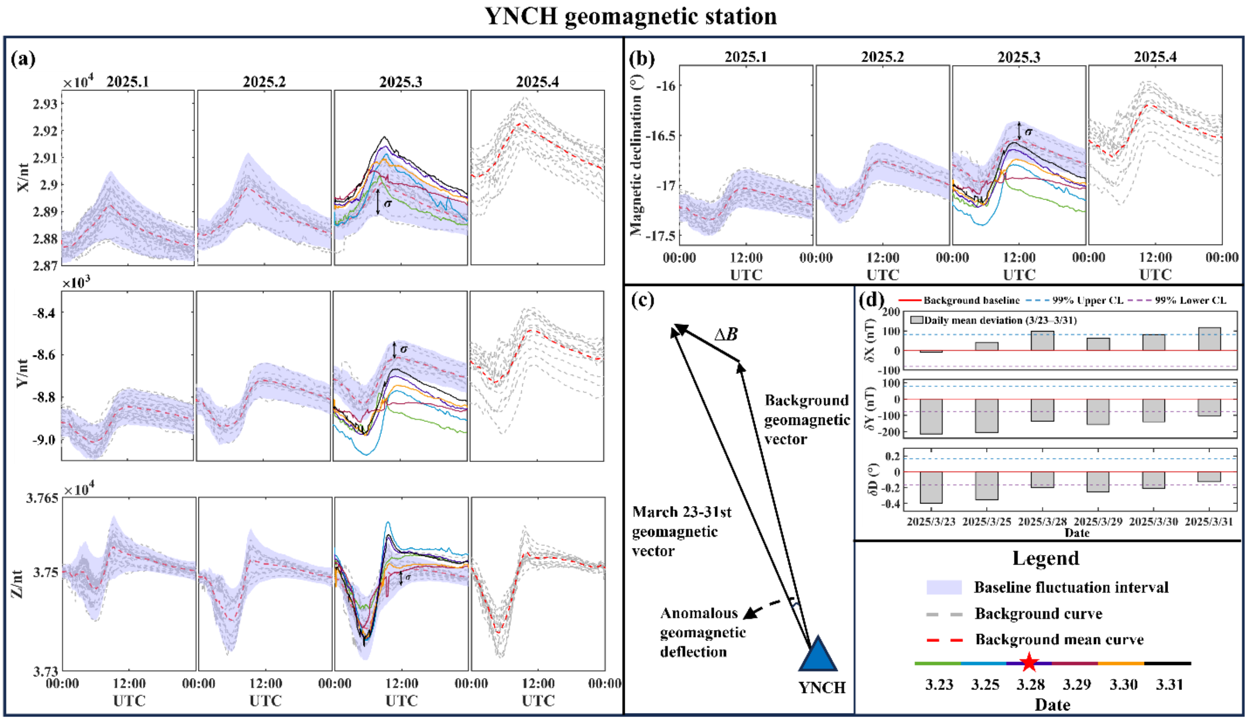

Figure 3: The variation in magnetic declination, X-, Y- and Z- component recorded by YNCH on Jan, Feb, Mar and April, 2025, respectively. The background curves and background mean curves were derived from geomagnetic data recorded in a month, subject to the criteria of Kp ≤ 4 and a cross-correlation coefficient correlation > 0.6. The background mean curve for March were calculated using geomagnetic data from March 1st to March 22nd (before the first anomaly). The σ were calculated by Eq. (1). The HVGD was calculated as follows: $\Delta B = \sqrt{\Delta X^2 + \Delta Y^2}$, and the magnetic declination was calculated as: $D = \arctan(Y/X)$. The daily mean deviation in (d) was obtained by averaging the differences between the curves on anomalous days (March 23rd to March 31st) and the background mean curve. The 99% Upper CL and 99% Lower CL were the upper and lower limits of the 99% confidence interval calculated based on the daily mean σ, respectively. During the period from March 23rd to March 31st, the deviations of the X-, Y- component and the magnetic declination from the background mean curve clearly exceeded the 99% confidence interval.

3.2 Intersection points along saging fault

Based on the geomagnetic observations from March 23 to 31 and the corresponding background field calculated from March 1 to March 22, the equations of the normal lines of HVGD were derived. A geometric parametric equation was established for each segment of Sagaing fault. Then, the intersection points were subsequently calculated by solving these two equations. To investigate the spatio-temporal and quantitative relations between the intersection points and the epicenters of earthquake sequence, a bar chart was constructed, as shown in Fig. 4, with each bar representing a segment along the fault at a latitudinal space of 0.5°.

https://doi.org/10.5194/egusphere-2026-4946
Preprint. Discussion started: 23 September 2026

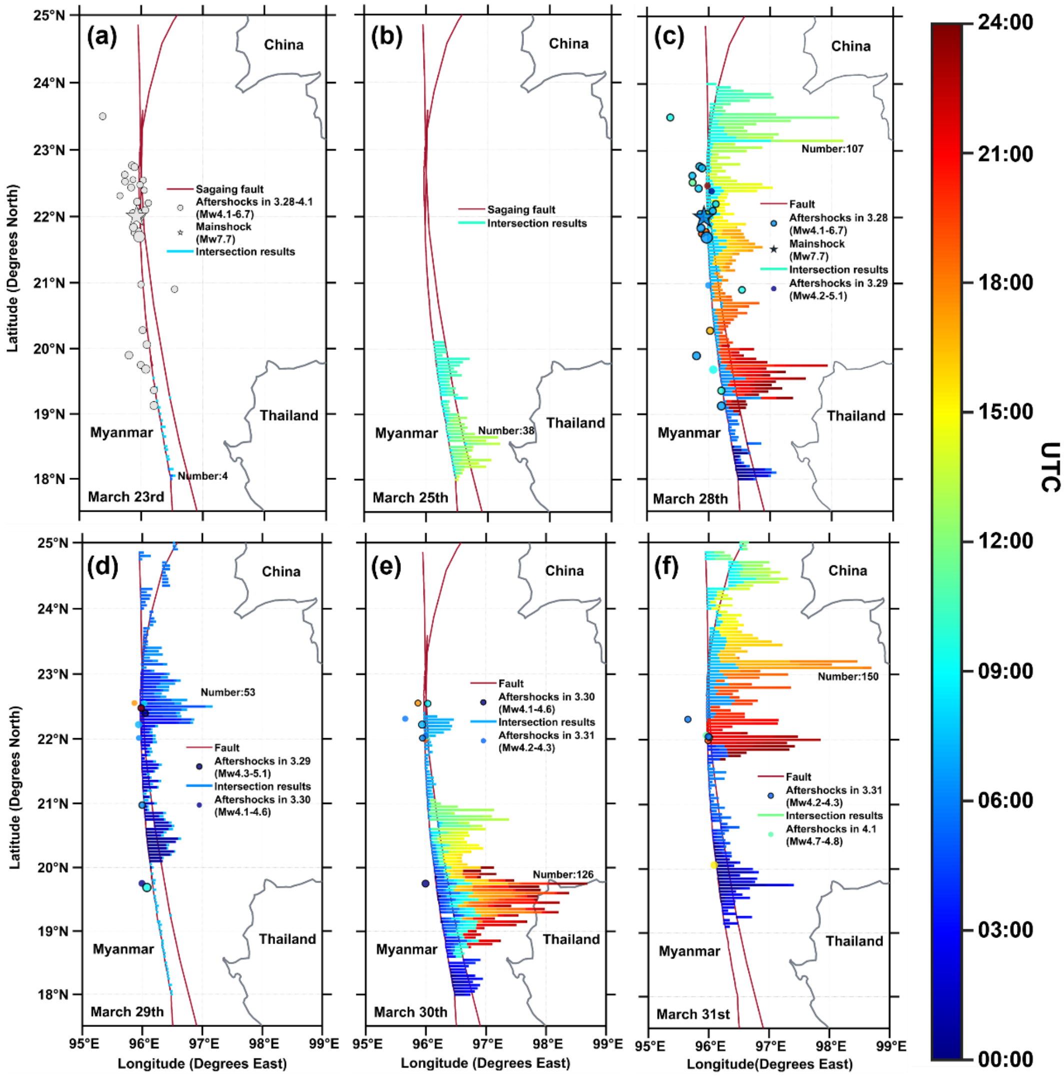

Figure 4: The spatio-temporal distribution of daily intersection points and the epicenters of earthquake sequence from March 23 to 31, 2025. The results are calculated by the developed simple forward spatial intersection method. The color of the intersection bars encodes time, while the color stacking indicates the persistent presence of intersections in this region across different time intervals. The length of intersection bars represents the quantity of intersection points. The label of number represents the max number of intersection points on the whole day. The color of each bar represents the time information of intersection points within a day, whereas the length of bar represents the total number of intersection points inside the segment on that day.

We discovered that a small number of intersection points started appearing sporadically in the southern segments of Sagaing fault on March 23rd, and the number of intersection points gradually increased until March 28th. With the occurrence of the mainshock on March 28th, the intersection points migrated toward the epicentral region, and subsequently shifted to where the aftershocks happening. The phenomenon indicates a strong spatio-temporal correlation between the earthquake epicenters and the intersection points. Later on March 29th, the intersection points further migrated northward to areas near

https://doi.org/10.5194/egusphere-2026-4946
Preprint. Discussion started: 23 September 2026

the epicenters of three aftershocks. Furthermore, the intersection points on March 30th and 31st demonstrated also strong spatio-temporal correlations with the corresponding aftershock epicenters.

This particular spatio-temporal pattern likely reflects an initial stage of regional stress accumulation in the southern segment of the fault, followed by northward stress migration and eventual stress release through seismic rupturing in the central segment. The initial regional stress accumulation in the southern segment of Sagaing fault could be attributed to the release of locked rock strain energy by the Mw 6.9 earthquake occurred at its northern segment in 2012 (Lindsey et al., 2025). The most recent major earthquakes happened in the southern segment of Sagaing fault were the 1929 Mw 6.6 and 1930 Mw 7.5 events, indicating a 95-years strain accumulation at the south segment (Wei et al., 2025). Therefore, the appearance of intersection points starting at the southern segment, followed by their migration toward the epicentral zone, may indicate indirectly the strain build-up and seismic rupture along the Sagaing fault.

On March 31st, the maximum number of intersection points at the segments of 0.5° space along the fault, as well as the entire fault, was greater than that on March 28th (see Supplementary Material-Fig. S7), this increase may be attributed to massive rock fracturing caused by the mainshock, which likely facilitated the massive production of P-holes and its upward migration to ground surface along the Sagaing fault.

Furthermore, the analysis of time periods with Kp ≤ 4 on March 24th, 26th, and 27th (see Supplementary Material-Fig. S8) reveals a higher concentration of intersection points on March 26th and 27th, as comparing to that on March 23rd. Notably, these intersection points are predominantly distributed in the southern fault segment, further indicating the pre-seismic stress accumulation in the southern fault segment.

In addition, positive anomalies in microwave brightness temperature (MBT) were proved closely correlated with the PSRC generated by earthquake (Qi et al., 2020; Qi et al., 2022; Ding et al., 2024). We conducted further a comprehensive analysis of MBT anomalies preceding and following the Mandalay earthquake (see Supplementary Material-Fig. S9 and Fig. S10). The results indicate that pre-seismic MBT positive anomalies were predominantly located to south of Sagaing fault, exhibiting a strong spatial relation with the distribution of magnetic intersection points. Post-seismically, the MBT anomalies became concentrated in areas characterized by high densities of magnetic intersection points, which shows a wonderful spatial consistency between the intersections and positive MBT anomalies.

3.3 Quantifying the magnitude of PSRC

Generally, P-holes are typically dormant and exist as pairs in the form of peroxy bonds (O–O), which are mainly associated with crust rock containing silicate minerals like feldspar, quartz and olivine (Freund, 2011). As shown in Fig. 1(b) and Fig. 1 (c), the seismogenic zone is adjacent to a volcanic arc. The local surface layer consists of Quaternary marsh deposits, underlain by Tertiary (N) igneous rocks, intrusive rocks, minor sedimentary rocks, and Cretaceous–Paleocene (K–E1) igneous bodies. The underlying bedrock is mainly composed of Cretaceous–Paleocene (K–E1) igneous complexes, predominantly diorite and andesite. Located at the convergence boundary between the Indian and Eurasian plates, the region around Sagaing fault has experienced significant intrusions of the Indian Plate, resulting in the formation of extensive

https://doi.org/10.5194/egusphere-2026-4946
Preprint. Discussion started: 23 September 2026

igneous and intrusive rocks such as andesite and diorite. These rocks are primarily composed of feldspars (plagioclase and K-feldspar), quartz, amphibole, and pyroxene. The abundance in silicate minerals makes them a good source of P-holes to be activated by crustal stress accumulated around the coming epicenters. In addition, both the relatively lower stress conditions near the ground surface and the widespread presence of Tertiary (N) and Cretaceous–Paleocene (K–E1) igneous mineral crystals are conducive to the upward migration of P-holes.

According to Fig. 2(b) and Biot-Savart law, the upward seismogenic PSRC can be retrieved with the induced magnetic horizontal disturbance recorded by magnetic station at ground surface as Eq. (2).

$$\mathrm{PSRC} = \Delta B \frac{4\pi a}{\mu}\left(\frac{\sqrt{H^2 + a^2}}{H}\right) \tag{2}$$

Where, H represents the length of PSRC, which also corresponds to the depth of the epicenter, ΔB is the PSRC induced magnetic horizontal disturbance, a is the distance from the YNCH station to the fault intersection point, μ is the magnetic permeability.

Using to the average hypocenter depth 30 km, and taking the magnetic permeability $\mu=4.16\pi\times10^{-7}$ H/m (See Supplementary Material-Text S4) be the approximate permeability of underground rock mass, the changing PSRCs correlated with the Mandalay earthquake sequences were quantitatively estimated (The detailed results are provided in Fig. 5 and Fig. 8a).

Furthermore, in order to investigate the spatio-temporal relationships between the epicenter, PSRC, and distance, the mainshock epicenter was taken as the reference, and the relative latitudinal distances (north-south offsets) of each intersection point and aftershocks from the mainshock epicenter were carefully calculated. The results are visualized in Fig. 5.

According to Fig. 5, the PSRC manifestations were broadly synchronous with the occurrence of earthquakes. Furthermore, the distances between the fault intersection points and the epicenters predominantly fell within the range of 0–300 km, with an average distance of 182 km. The PSRC reached its maximum on March 26th, peaking at 91.9 MA. Notably, the average distance between the intersection points identified on Marth 26th and the two major earthquakes (Mw 7.7 and Mw 6.7) that occurred on Marth 28th was only about 100 km. Meanwhile, the PSRC began to decline from March 28th to 29th, dropping to a minimum of 7.3 MA. Subsequently, it increased again from March 30th to 31st. This interesting pattern may be attributed to the numerous fractures generated during the initial seismic rupture, which created favorable pathways for the transmission of P-holes. This interpretation is consistent with recent experimental observations (Sun et al., 2025).

https://doi.org/10.5194/egusphere-2026-4946
Preprint. Discussion started: 23 September 2026

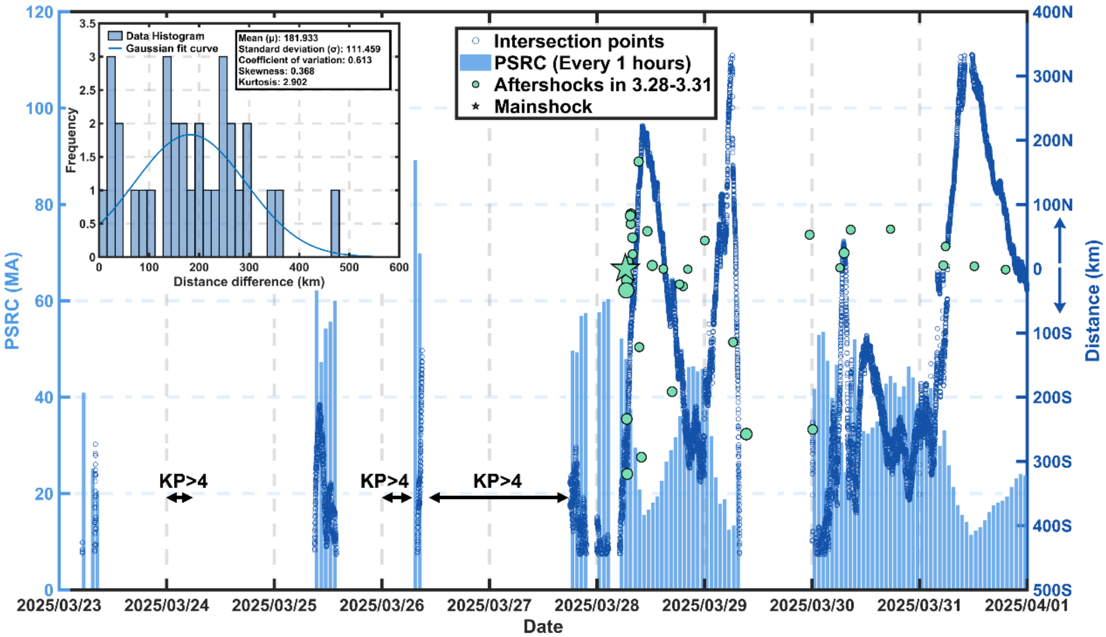

Figure 5: Variation of estimated PSRCs and distances of intersection points produced from Marth 23rd to 31st, 2025. Distances for aftershocks and intersection points are defined relative to the location of mainshock. The subplot presents the statistical distribution (histograms) of distances between intersection points and epicenters at the time of each earthquake (mainshock and aftershocks).

4 Discussion

4.1 Relationship Between HVGD-Inferred Positions and Supershear Rupture Along the Sagaing Fault

The overlap between the pre-mainshock HVGD-inferred locations and the subsequent supershear rupture segment is particularly notable. Recent seismic and geodetic studies indicate that the 2025 Mandalay earthquake ruptured approximately 475–510 km of the Sagaing fault, including a long southern segment that propagated at a supershear speed (Xu et al., 2025; Wei et al., 2025; Dara et al., 2025; Li et al., 2025). These studies consistently place the onset of supershear ruputure approximately 100 km south of the mainshock epicenter, although its inferred southward extent varies from 200 km to 350 km (see Fig. 6). These estimaged segments largely overlap the pre-mainshock region HVGD–fault intersection points that were predominantly distributed between 18°N and 21°N.

Within the PSRC framework, this spatial correspondence may reflect stress-related electrical activation along the southern fault segment and indicate the development of a highly stressed region at depth. Supershear rupture is generally favored by mechanical conditions such as high prestress, low fracture energy, and strong dynamic stress concentration along a mature, geometrically continuous fault segment (Xu et al., 2015). Although the present observations do not establish a direct causal relationship between PSRC generation and supershear rupture, they suggest that the southern Sagaing Fault may have already been in a mechanically favorable state before the mainshock. The northern part of the HVGD-inferred region extends beyond the identified supershear segment, possibly indicating elevated pre-mainshock stress that was insufficient, or

https://doi.org/10.5194/egusphere-2026-4946
Preprint. Discussion started: 23 September 2026

otherwise mechanically unfavorable, to support supershear rupture. Therefore, the HVGD-derived intersections may provide independent electromagnetic evidence for stress activation along the segment that subsequently hosted supershear rupture along active fault, at least for Sagaing Fault.

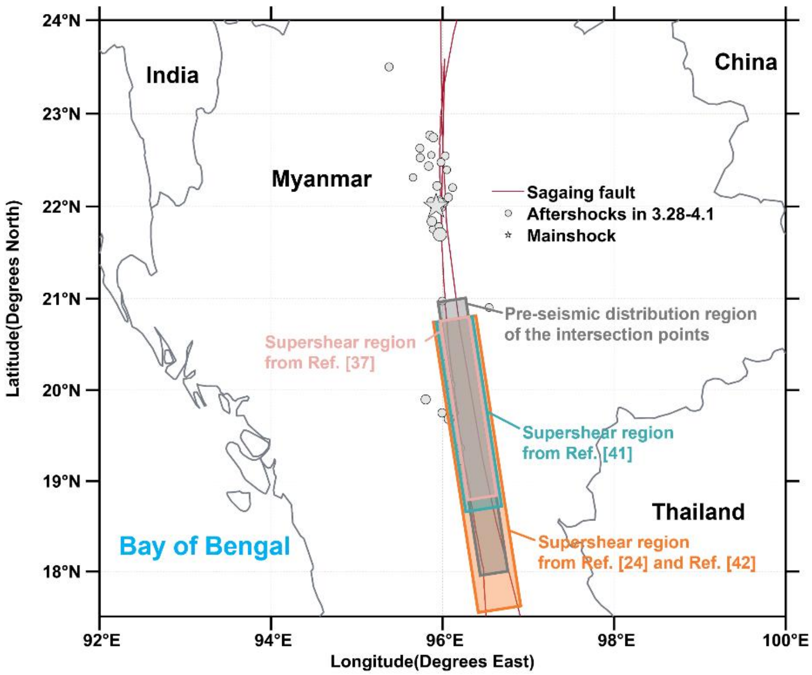

Figure 6: Spatial distribution of the supershear rupture and pre-seismic intersection points. The corresponding latitude ranges for the onset of supershear rupture from each research were as follows: 18.71°N–20.74°N (100 km–325 km) **(**Dara et al., 2025**)**; 18.94°N–20.74°N (100 km–450 km) **(**Xu et al., 2025; Li et al., 2025**)**; Research 3: 17.58°N–20.74°N (100 km–300 km) **(**Wei et al., 2025**)**. The pre-seismic intersection points were predominantly concentrated within the latitudinal range of 18°N–21°N (see Fig. 4 and Supplementary Material-Fig. S8).

4.2 Relationship Between HVGD-Inferred Positions and Supershear Rupture Along the Sagaing Fault

The MBT analysis was based on the satellite overpass time of 1:30 am local time. Converted from Myanmar local time to UTC, this corresponds to 7:00 pm on the previous day. Therefore, the MBT anomaly of March 28th was considered post-seismic anomaly and was excluded from the calculation of the pre-seismic anomaly area. Accordingly, the mean pre-seismic PSRC was calculated for the period from March 23 to March 27 (see Fig. 7a and 7b), yielding a value of 50.4 MA. During the same period, the mean area of positive MBT anomalies was determined to be 1,557.7 km² (see Fig. 7c and 7d); detailed calculation procedures of the MBT anomaly area see Supplementary Material-Text S5. Based on the calculated mean PSRC and anomaly area, the possible pre-seismic PSRC density was estimated to be 32.3 mA/m².

The estimated pre-seismic PSRC density is approximately 32.3 mA/m². Although this PSRC density is negligible to human beings during routine activities (direct dermal contact is virtually absent), it mab be relevant for animals that maintain direct contact with the ground or inhabit shallow subsurface environments, particularly burrowing specie (Cordeiro de Sousa & Hoffmann, 1985; Lunsford et al., 2022; Chuang et al., 2011). This finding provides a possible physical basis for interpreting

https://doi.org/10.5194/egusphere-2026-4946
Preprint. Discussion started: 23 September 2026

some forms of pre-seismic unusual animal behavior as responses to near-surface electrical disturbances. In this scenario, upward-propagating stress-activated charge carriers could produce weak but biologically perceptible electric currents near the ground surface. Such currents may induce discomfort or behavioral changes in animals sensitive to electrical stimulation. This interpretation remains hypothetical, but it is consistent with the field observations reports showing that some animals respond to weak electric currents. Besides, the occurrence of large pre-seismic PRSCs, as shown in Fig. 6 and 8a, may also have implications for regional earthquake lights (EQLs). If locally concentrated electric currents or charge accumulation generate sufficiently strong electric fields near the surface, they could promote air ionization or corona-like discharge, potentially producing luminous phenomena. Thus, the PSRC mechanism may provide a unified framework for interpreting both geomagnetic disturbances and some macroscopic electromagnetic phenomena, such as EQLs, although direct observational confirmation remains necessary.

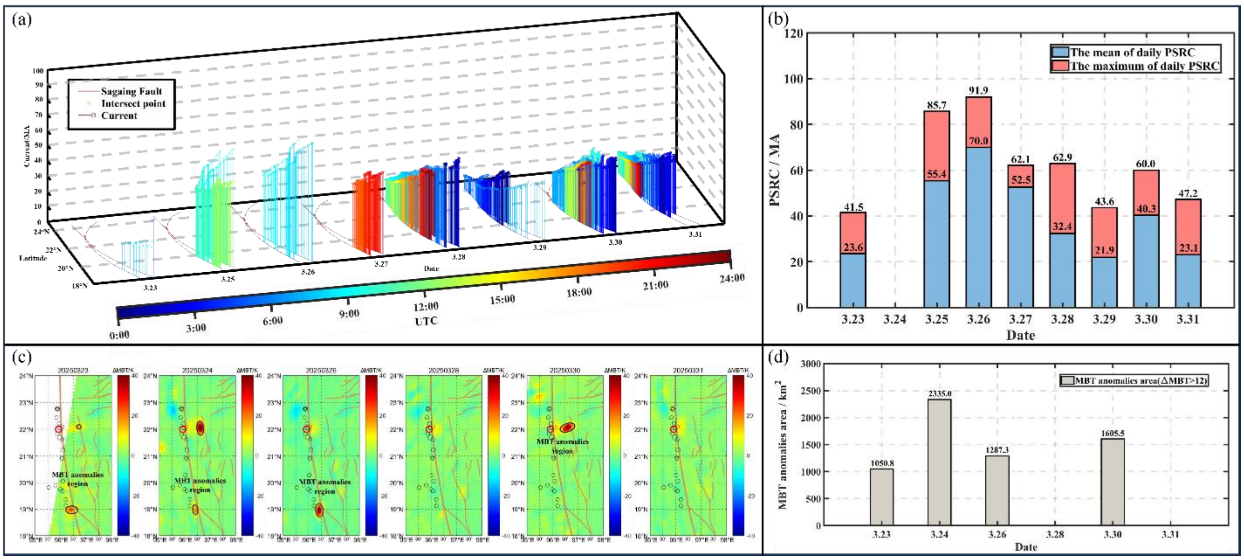

Figure 7: Distribution characteristics of PSRC and MBT anomaly regions. (a) PSRC calculation results of every intersection point. (b) Daily mean and maximum of PSRC. (c) MBT positive anomaly regions (The region of $\Delta MBT > 12$). (d) The area of MBT positive anomaly regions from March 23rd to March 31st.

Unusual animal behavior and earthquake lights have been reported in association with many large earthquakes. Examples include the exodus of toads before the Mw 6.3 earthquake in Italy (Grant et al., 2011), the earthworms emerging from the soil and rats exhibiting lethargy and sluggishness before the 2008 Wenchuan earthquake (Li et al., 2009; Che et al., 2008). EQLs phenomena have also been reported during or near several events such as the 2022 Fukushima (Xie et al., 2023), 1995 Kobe (Kamogawa et al., 2005), and 2009 Aquila earthquakes (Fidani, 2010). Biological studies indicate that toads, rats, and earthworms possess a high sensitivity to weak electric currents (McConville et al., 2006; Wang et al., 2022). The experiments show that toads exhibit significant avoidance behavior when exposed to currents ranging from 0.05-0.5 mA (McConville et al., 2006), and intermittent electrical stimulation at 1.29 mA induces discomfort and prompts them to burrow

https://doi.org/10.5194/egusphere-2026-4946
Preprint. Discussion started: 23 September 2026

out of the ground (Wang et al., 2022). These observations suggest that anomalous animal behavior may represent a macroscopic response to near-surface electrical disturbances during earthquake preparation.

For the 2025 Mandalay earthquake, the estimated mean PSRC density of 32.3 mA/m² implies that, for an animal with an effective ground contact area of approximately 0.003 m², the current passing through the body could be on the order of 0.1 mA. This value falls within the range that may be biologically perceptible for some electrically sensitive animals. Because this estimate is based on the mean PSRC intensity and the mean area of the microwave brightness temperature anomaly, the instantaneous and local current density could have been higher than the mean value. Therefore, unusual animal behavior may have occurred before the 2025 Mw 7.7 Mandalay earthquake but may have gone unreported, unnoticed, or undocumented. Nevertheless, this interpretation should be regarded as a plausible implication rather than a direct conclusion. Animal behavior is influenced by many environmental, ecological, and anthropogenic factors, and retrospective reports are often incomplete or difficult to verify. Future studies combining continuous electromagnetic monitoring, satellite thermal or microwave observations, and systematic biological or public-report datasets would be required to test the proposed relationship.

4.3 Potential and Limitations of Remote HVGD Monitoring

This study suggests that remotely observed HVGD may contain useful directional information related to seismogenic processes. When the geometry of an active fault is known, the intersection between the fault trace and the normal lines of HVGD vectors recorded at a remote geomagnetic station may help constrain the segment where stress-related electric currents are generated. In the case of the 2025 Mandalay earthquake sequence, this approach identified a series of positions along the Sagaing Fault that were spatially consistent with the rupture corridor and major events of the earthquake sequence.

If the causative fault is unknown or multiple active faults exist in the monitored region, observations from a single geomagnetic station are generally insufficient to uniquely determine the source region. In such cases, simultaneous HVGD observations from two or more geomagnetic stations at different locations would be required to triangulate the possible seismogenic zone. Integration with independent datasets, such as satellite microwave brightness temperature, ionospheric observations, surface deformation, seismicity migration, and public reports of macroscopic anomalies, could further improve the reliability of source-region constraints.

However, several limitations should be emphasized. First, geomagnetic disturbances can be influenced by external space-weather activity, magnetospheric and ionospheric currents, cultural noise, and local electromagnetic interference. Careful preprocessing and exclusion of non-seismic sources are therefore essential. Second, the HVGD–fault intersection method depends on the assumed geometry of the mapped fault. Errors or simplifications in the fault trace may affect the inferred intersection positions. Third, the conversion from observed geomagnetic disturbance to PSRC intensity using the Biot–Savart law involves simplifying assumptions regarding current geometry, source depth, and conductivity structure. Fourth, the relationship between estimated PSRC intensity and earthquake magnitude or strain energy release remains poorly constrained and likely depends on lithology, stress state, fault maturity, fluid content, and crustal conductivity.

Therefore, while HVGD monitoring may provide valuable information on the direction and migration of stress-related electromagnetic sources, it should not be interpreted as a standalone deterministic earthquake prediction tool. Instead, it is better viewed as a complementary geophysical method for tracking possible electromagnetic manifestations of seismogenic processes along active faults.

5 Conclusions

This study analyzed geomagnetic disturbances recorded at the remote YNCH station during the 2025 Mw 7.7 Mandalay earthquake sequence and developed an HVGD–fault intersection method to investigate their spatial relationship with the Sagaing Fault. Lines normal to the horizontal vectors of geomagnetic disturbance (HVGD) intersected the mapped fault trace at locations broadly corresponding to the rupture corridor and major earthquakes. Before the mainshock, the intersections were concentrated along the southern Sagaing Fault between 18°N and 21°N, overlapping the segment subsequently identified as having hosted supershear rupture. This correspondence suggests that the remotely observed HVGD contained directional information related to stress-associated electromagnetic processes along the fault.

The inferred equivalent pressure-stimulated rock currents (PSRCs) ranged from 7.3 to 91.9 MA, comparable in magnitude to estimates obtained by scaling laboratory measurements to seismogenic rock volumes. This agreement supports PSRCs generated in stressed, peroxy-defect-bearing rocks as a plausible, but not unique, source of the observed disturbances. Satellite-observed microwave brightness temperature anomalies showed complementary spatial correspondence with the HVGD-inferred regions, although the physical relationship between these observations remains to be established.

Overall, combining remote HVGD observations with mapped fault geometry provides a simple, testable approach for constraining candidate electromagnetic source locations and their apparent migration along an active fault. Further evaluation requires observations from multiple stations and earthquake sequences, rigorous separation of tectonic and external geomagnetic signals, and improved modeling of source geometry and three-dimensional crustal conductivity.

Code and data availability

The global active faults data used in this paper are available from Global Earthquake Model Foundation (2019). The Myanmar earthquake sequences were collected from the United States Geological Survey (USGS). The DEM data were downloaded from the General Bathymetric Chart of the Oceans (GEBCO) (GEBCO Compilation Group, 2023). The Kp index data were downloaded from the Helmholtz Centre for Geosciences (GFZ) (Matzka et al., 2021). Geomagnetic data collected at the YNCH station are available from (Feng et al., 2026).

Supplement link

The Supplement is shown in Supplementary Material.

Author contributions

Conceptualization: Lixin Wu, Wenfei Mao
Data curation: Yu Feng, Wenfei Mao
Formal analysis: Yu Feng, Yifan Ding, Yuan Qi, Licheng Sun
Funding acquisition: Wenfei Mao, Lixin Wu
Investigation: Lixin Wu, Wenfei Mao, Yu Feng, Busheng Xie, Guokun Chen, Hong Tang, Licheng Sun
Methodology: Lixin Wu, Wenfei Mao
Supervision: Lixin Wu, Wenfei Mao, Jia Li
Writing – original draft: Yu Feng

Competing interests

The authors declare no conflicts of interest relevant to this study.

Acknowledgements

This work was jointly supported by the National Key Research and Development Program of China under Grant 2023YFE0208000, the State Key Program of National Natural Science Foundation of China (grant no. 41930108) and the National Basic Research Program of China (973 Program) (Grant No.2011CB707102).

References

Che, Y., Liu, C., Yu, J., Guan, Z., & Li, J. Underground fluid anomaly and macro anomaly of the Ms 8.0 Wenchuan earthquake and options about earthquake prediction. Seismol. Geol. 30, 828–838 (2008). (in chinese)

Chen, J., Xu, M., Bai, Y., Wu, S., Xiao, X., Hao, S., Nagaso, M., Yang, H. & Tong, P. High normal stress promoted supershear rupture during the 2023 Mw 7.8 Kahramanmaraş earthquake. Nat. Geosci. 19, 223–230 (2026). https://doi.org/10.1038/s41561-025-01893-z

Chernogor, L. Geomagnetic Disturbances Accompanying the Great Japanese Earthquake of March 11, 2011. Geomagn. Aeron. 59, 62–75 (2019). https://doi.org/10.1134/S0016793219010043

Chuang, H., Raizen, D., Dabbish, N. & Bau, H. Electro-worming: The behaviors of Caenorhabditis (C.) elegans in DC and AC electric fields. Physics of Fluids. 23, 91107-911071 (2011). https://doi.org/10.1063/1.3640009

Cordeiro de Sousa, M. & Hoffmann, A. Autonomic adjustments during avoidance and orienting responses induced by electrical stimulation of the central nervous system in toads (Bufo paracnemis). J. Comp. Physiol. B. 155, 381–386 (1985). https://doi.org/10.1007/BF00687482

Ding, Y., Wu, L., Qi, Y. & Mao, W. Discriminating the polymorphism and attribution of microwave radiation anomalies related to the June 2022 Mw 6.0 Paktika earthquake in Afghanistan. Natl Remote Sens. Bull. 28, 2621–2631 (2024). https://doi.org/10.11834/jrs.20243019 (in chinese)

Enomoto, Y., Heki, K., Yamabe, T., Sugiura, S. & Kondo, H. A possible causal mechanism of geomagnetic variations as observed immediately before and after the 2011 Tohoku-Oki earthquake. Open J. Earthq. Res. 9, 33–49 (2020). https://doi.org/10.4236/OJER.2020.92003

Feng, Y., Wu, L., Mao, W., Li, J., Ding, Y., Qi, Y., Chen, G., Xie, B., Sun, L. & Tang, H. (2026). Remote HVGD Implying the Seismogenic Positions of 2025 Mandalay Earthquake Sequence (Version v1) [Dataset]. Zenodo. https://doi.org/10.5281/zenodo.21129007

Fidani, C. The earthquake lights (EQL) of the 6 April 2009 Aquila earthquake, in central Italy. Nat. Hazards Earth Syst. Sci. 10, 967–978 (2010). https://doi.org/10.5194/nhess-10-967-2010

Freund, F. Pre-earthquake signals: Underlying physical processes. J. Asian Earth Sci. 41, 383–400 (2011). https://doi.org/10.1016/j.jseaes.2010.03.009

Freund, F. T., Takeuchi, A. & Lau, B. Electric currents streaming out of stressed igneous rocks – A step towards understanding pre-earthquake low frequency EM emissions. Phys. Chem. Earth Parts A/B/C. 31, 389–396 (2006). https://doi.org/10.1016/j.pce.2006.02.027

Gao, H. & Yin, L. Discuss on the correlations between landslides and rainfall and threshold for landslide early-warning and prediction. Rock and Soil Mechanics 28, 1055–1060 (2007). (in chinese)

GEBCO Compilation Group. (2023). GEBCO 2023 Grid [Dataset]. https://doi.org/10.5285/f98b053b-0cbc-6c23-e053-6c86abc0af7b

Global Earthquake Model Foundation. (2019). GEMScienceTools/gem-global-active-faults: First release of 2019 (Version 2019.0) [Dataset]. Zenodo. https://doi.org/10.5281/zenodo.3376300

Goldberg, D., Yeck, W, Hanagan, C., Atterholt, J., Kehoe, H., Reitman, N., Barnhart, W., Shelly, D, Hatem, A, Wald, D., & Earle, P. Ultralong, supershear rupture of the 2025 Mw 7.7 Mandalay earthquake reveals unaccounted risk. Science. 390,458-462 (2025). https://doi.org/10.1126/science.ady3581

Grant, R., Halliday, T., Balderer, W., Leuenberger, F., Newcomer, M., Cyr, C. & Freund, F. Ground water chemistry changes before major earthquakes and possible effects on animals. Int. J. Environ. Res. Public Health. 8, 1936–1956 (2011). https://doi.org/10.3390/ijerph8061936

https://doi.org/10.5194/egusphere-2026-4946
Preprint. Discussion started: 23 September 2026

Guan, Y., Dong, X., Feng, L., He, M. & Ji, Y. Remarkable variations in geomagnetic disturbances preceding the 2017 M 7.1 Jiuzhaigou earthquake. Phys. Earth Planet. Inter. 368, 107438 (2025). https://doi.org/10.1016/j.pepi.2025.107438

Hamidi, M., Ahadi, S., Friska, V. & Marzuki, M. Investigating ultra-low frequency emissions and total electron content anomalies as earthquake precursors in Sumatra (2019–2020). Kuwait J. Sci. 51, 100196 (2024). https://doi.org/10.1016/j.kjs.2024.100196

Hattori, K., Han, P., Yoshino, C., Febriani, F., Yamaguchi, H. & Chen, C. Investigation of ULF seismo-magnetic phenomena in Kanto, Japan during 2000–2010: Case studies and statistical studies. Surv. Geophys. 34, 293–316 (2013). https://doi.org/10.1007/s10712-012-9215-x

Kamogawa, M., Ofuruton, H. & Ohtsuki, Y. Earthquake light: 1995 Kobe earthquake in Japan. Atmos. Res. 76, 438–444 (2005). https://doi.org/10.1016/j.atmosres.2004.11.018

Kosuke Heki & Wei Zhan. Ionospheric changes immediately before the 2025 March 28 Mw 7.7 Myanmar earthquake. Geophys. J. Int. 245, ggag124 (2026). https://doi.org/10.1093/gji/ggag124

Li, B., Jonsson, S., Suhendi, C., Liu, J., Li, D., Delorme, A., Klinger, Y., & Mai, P. Seismic gap breached by the 2025 Mw 7.7 Mandalay (Myanmar) earthquake. Nat. Geosci. 18, 1287–1295 (2025). https://doi.org/10.1038/s41561-025-01861-7

Li, Y., Liu, Y., Jiang, Z., Guan, J., Yi, G., Cheng, S., Yang, B., Fu, T. & Wang, Z. Behavioral change related to Wenchuan devastating earthquake in mice. Bioelectromagnetics. 30, 613–620 (2009). https://doi.org/10.1002/bem.20520

Liang, G. Preliminary study of the relationship between cryptoexplosion and ore-forming process from Wenchuan earthquake. Acta Petrol. Sin. 33, 326–338 (2017). (in chinese)

Lindsey, E., Kuo, Y., Wang, Y., Thant, M. & Tha Zin Htet Tin. Mature fault mechanics revealed by the highly efficient 2025 Mandalay earthquake. Nat Commun. 16, 10937 (2025). https://doi.org/10.1038/s41467-025-65942-2

Lunsford, E., Paz, A., Keene, A. & Liao, J. Evolutionary convergence of a neural mechanism in the cavefish lateral line system. eLife. 11, e77387 (2022). https://doi.org/10.7554/eLife.77387

Mao, W., Wu, L., Xu, Y., Yao, R., Lu, J., Sun, L. & Qi, Y. Pressure-stimulated rock current as loading diorite to failure: Particular variation and holistic mechanisms. J. Geophys. Res. Solid Earth. 127, e2022JB024931 (2022). https://doi.org/10.1029/2022JB024931

Mao, Z., Chen, C., Yen, H., Chen, Y., Zhang, P., Zhang, S., Sun, Y., Han, P., Wu, C., Gao, Y., Rapoport, Y., Lin, C., Liu, J. & Yu, H. Near-field temporal electric current after the 2024 Mw 7.4 Hualien earthquake. Geomat. Nat. Hazards Risk. 16, 2595695 (2025). https://doi.org/10.1080/19475705.2025.2595695

Matzka, J., Bronkalla, O., Tornow, K., Elger, K., & Stolle, C. (2021). Geomagnetic Kp index (Version 1.0) [Dataset]. GFZ Data Services. https://doi.org/10.5880/Kp.0001

Maurin, T., Masson, F., Rangin, C., Min, UT. & Collard, P. First global positioning system results in northern Myanmar: Constant and localized slip rate along the Sagaing fault. Geology. 38, 591–594 (2010). https://doi.org/10.1130/G30872.1

McConville, J., Sterritt, L., & Laming, P. Behavioural responses to electrical and visual stimulation of the toad tectum. Behav. Brain Res. 170, 15-22 (2006). https://doi.org/10.1016/j.bbr.2006.01.027

https://doi.org/10.5194/egusphere-2026-4946
Preprint. Discussion started: 23 September 2026

Qi, Y., Wu, L., Ding, Y., Liu, Y., Wang, X. & Mao, W. Microwave brightness temperature (MBT) background in Bayan Har Block, Qinghai-Tibet Plateau and its importance in searching for seismic MBT anomalies. Remote Sens. 14, 534 (2022). https://doi.org/10.3390/rs14030534

Qi, Y., Wu, L., Mao, W., Ding, Y. & He, M. Discriminating possible causes of microwave brightness temperature positive anomalies related with May 2008 Wenchuan earthquake sequence. IEEE Trans. Geosci. Remote Sens. 59, 1903–1916 (2020). https://doi.org/10.1109/TGRS.2020.3004404

Ren, J., Niu, B., Wang, J., Jin, X., Zhao, L. & Liu, R. Advances in research of Asian geology—A summary of 1:5M International Geological Map of Asia project. J. Asian Earth Sci. 72, 3–11 (2013). https://doi.org/10.1016/j.jseaes.2013.02.006

Socquet, A., Vigny, C., Chamot-Rooke, N., Simons, W., Rangin, C. & Ambrosius, B. India and Sunda plates motion and deformation along their boundary in Myanmar determined by GPS. J. Geophys. Res. Solid Earth. 111, B05406 (2006). https://doi.org/10.1029/2005JB003877

Sun, L., Wu, L., Xu, Y., Dong, G, Zheng, T. & Mao, W. Characteristics and spatial differences of pressure-stimulated rock potential in diorite partly loaded to fracturing. Int. J. Rock Mech. Min. Sci. 196, 106328 (2025). https://doi.org/10.1016/j.ijrmms.2025.106328

Sun, L., Wu, L., Xu, Y., Zheng, T., Dong, G., Wang, Z. & Mao, W. Sustaining post-peak pressure-stimulated rock current from bi-axially loaded sandstone and diorite specimens. Rock Mech. Rock Eng. 59, 87–103 (2026). https://doi.org/10.1007/s00603-025-04880-3

Syed Zafar, S., Umar, R., Sabri, N., Jusoh, M., Yoshikawa, A., Abe, S. & Uozumi, T. A statistical analysis of the relationship between Pc4 and Pc5 ULF waves, solar winds and geomagnetic storms for predicting earthquake precursor signatures in low latitude regions. IOP Conf. Ser. Earth Environ. Sci. 880, 012010 (2021). https://doi.org/10.1088/1755-1315/880/1/012010

Takla, E., Yumoto, K., Ishitsuka, J., Rosales, D., Dutra, S., Uozumi, T. & Abe, S. Geomagnetic variations possibly associated with the Pisco earthquake on 15 August 2007, Peru. Tectonophysics. 524–525, 29–36 (2012). https://doi.org/10.1016/j.tecto.2011.12.008

Tapponnier, P., Peltzer, G., Le Dain, A., Armijo, R. & Cobbold, P. Propagating extrusion tectonics in Asia: New insights from simple experiments with plasticine. Geology. 10, 611–616 (1982). https://doi.org/10.1130/0091-7613(1982)10<611:PETIAN>2.0.CO;2

The New York Times. Earthquake in Portugal: Graphic description of a recent earthquake. (1858, 10-25).

United States Geological Survey (USGS). (n.d.). Earthquake Catalog [Dataset]. https://earthquake.usgs.gov/earthquakes/map/

Vigny, C., Socquet, A., Rangin, C., Chamot Rooke, N., Pubellier M., Bouin M., Bertrand, G. & Becker, M. Present-day crustal deformation around Sagaing fault, Myanmar. J. Geophys. Res. Solid Earth. 108, 2533 (2003). https://doi.org/10.1029/2002JB001999

Volvach, A., Kurbasova, G. & Volvach, L. Parametric resonance of surface geomagnetic waves as a precursor of local earthquakes. Phys. Chem. Earth Parts A/B/C. 137, 103802 (2025). https://doi.org/10.1016/j.pce.2024.103802

Wang, H., Cheng, Y., Jin, M., Meng, X., Shi, L., Shen, M. & Lu, C. Responses of earthworm to the electric stimulation and the parameter quantification of its stress separation from earthworm dung. Trans. Chin. Soc. Agric. Eng. 38, 184–192 (2022). https://doi.org/10.11975/j.issn.1002-6819.2022.06.021 (in chinese)

Wei, S., Wang, X., Li, C., Zeng, H., Ma, Z., Shi, Q., Chen, H., Shi, Q., Chen, H., Huang, Y., Lyu, M., Liao, J., Yang, S., Bai, Y., Phyo Maung Maung., Kyawmoe Oo., Yin Myo Min Htwe., Zhang, J., Luca Dal Zilio., Shan, X. & Chen L. Supershear rupture sustained through a thick fault zone in the 2025 Mw 7.8 Mandalay earthquake. Science. 390, 468-475 (2025). https://doi.org/10.1126/science.adz2101

Xie, B., Wu, L., Mao, W., Wang, Z., Sun, L. & Xu, Y. Horizontal magnetic anomaly accompanying the co-seismic earthquake light of the M7.3 Fukushima earthquake of 16 March 2022: Phenomenon and mechanism. Remote Sens. 15, 5052 (2023). https://doi.org/10.3390/rs15205052

Xie, B., Wu, L., Sun, L., Xu, Y., Yoshikawa, A. & Mao, W. Mechanism of multiple anomalies prior to Japan earthquakes from 2021 to 2023: Lithosphere–coversphere–atmosphere–ionosphere coupling driven by pressure-stimulated rock current. Earth Space Sci. 12, e2025EA004320 (2025). https://doi.org/10.1029/2025EA004320

Xie, B., Wu, L., Sun, L., Xu, Y., Yoshikawa, A. & Mao, W. Multi-mode pre-seismic geomagnetic anomalies reveal potential mechanisms of the August 15, 2007, Mw8.0 Pisco earthquake: Pressure-stimulated rock current. Tectonophysics. 922, 231065 (2026). https://doi.org/10.1016/j.tecto.2025.231065

Xie, N., Jiang, Y., Zhu, G., Yang, S., Li, A. & Zhang, K. Evolution of the Sagaing strike-slip fault and its control of Shwebo Basin structural evolution, Myanmar. Geoscience. 24, 268–272 (2010). (in chinese)

Xu, J., Zhang, H. & Chen, X. Rupture phase diagrams for a planar fault in 3-D full-space and half-space. Geophys. J. Int. 202, 2194-2206 (2015). https://doi.org/10.1093/gji/ggv284

Xu, L., Meng, L., Zhang, Y., Yang, Y., Wang, Y., Hu, C., Weng, H., Xu, W., Su, E. & Ji, C. Bimaterial effect and favorable energy ratio enabled supershear rupture in the 2025 Mandalay earthquake. Science. 390, 476-481 (2025). https://doi.org/10.1126/science.ady6100

Yusof, K., Abdullah, M., Hamid, N., Ahadi, S. & Ghamry, E. Statistical global investigation of pre-earthquake anomalous geomagnetic diurnal variation using superposed epoch analysis. IEEE Trans. Geosci. Remote Sens. 60, 1–13 (2022). https://doi.org/10.1109/TGRS.2021.3093555

Zhang, L., Fan, W., Ding, L., Ducea, M., Pullen, A., Li, J., Sun, Y., Yue, Y., Cai, F., Wang, C., Peng, T. & Sein, K. Quaternary volcanism in Myanmar: A record of Indian slab tearing in a transition zone from oceanic to continental subduction. Geochem. Geophys. Geosyst. 21, e2020GC009091 (2020). https://doi.org/10.1029/2020GC009091

Zhao, B., Taucer, F. & Rossetto, T. Field investigation on the performance of building structures during the 12 May 2008 Wenchuan earthquake in China. Eng. Struct. 31, 1707–1723 (2009). https://doi.org/10.1016/j.engstruct.2009.02.039

Zulhamidia, N., Abdullah, M., Hamid, N. & Yusof, K. Comparative analysis of variants of geomagnetic diurnal variation ratio method for earthquake precursor detection. J. Kejuruteraan. 35, 881–888 (2023). https://doi.org/10.17576/jkukm-2023-35(4)-10